Poincaré Plot Image and Rhythm–Specific Atlas for Atrial Bigeminy and Atrial Fibrillation Detection

Guadalupe García-Isla, Valentina Corino, and Luca Mainardi, *Member, IEEE*

***Abstract*—A detector based only on RR intervals capable of classifying other tachyarrhythmias in addition to atrial fibrillation (AF) could improve cardiac monitoring. In this paper a new classification method based in a 2D non-linear RRI dynamics representation is presented. For this aim, the concepts of Poincaré Images and Atlases are introduced. Three cardiac rhythms were targeted: Normal sinus rhythm (NSR), AF and atrial bigeminy (AB). Three Physionet open source databases were used. Poincaré Images were generated for all signals using different Poincaré plot configurations: RR, dRR and $RRdRR$. The study was computed for different time window lengths and bin sizes. For each rhythm, the Poincaré Images of the 80% of that rhythm's patients were used to create a reference image, a Poincaré Atlas. The remaining 20% were used as test and classified into one of the three rhythms using normalized mutual information and 2D correlation. The process was iterated in a tenfold cross-validation and patient-wise dataset division. Sensitivity results obtained for $RRdRR$ configuration and bin size 40 ms, for a 60 s time window were 94.35%±3.68, 82.07%±9.18 and 88.86%±12.79 with a specificity of 85.52%±7.46, 95.91%±3.14, 96.10%±2.25 for AF, NSR and AB respectively. Results suggest that a rhythm's general RRI pattern may be captured using Poincaré Atlases and that these can be used to classify other signal segments using Poincaré Images. In contrast with other studies, the former method could be generalized to more cardiac rhythms and does not depend on rhythm-specific thresholds.**

***Index Terms*—Atrial fibrillation (AF), Atrial bigeminy (AB), Normalized mutual information (NMI), 2D Correlation, Rhythm classification.**

I. Introduction

CARDIAC tachyarrhythmias refer to a group of pathological depolarization patterns that may occur both in the ventricles and in the atria. Although supraventricular tachyarrhythmias do not represent an explicit life-threatening risk, they are associated with high mortality and increased morbidity. Atrial tachyarrhythmias like atrial fibrillation (AF), atrial flutter (AFL) and atrial tachycardia (AT) are linked to thromboembolic events and myocardial tissue deterioration [1]. Their monitoring is thus, important to evaluate their occurrence and burden in order to apply the necessary treatment and follow its effectiveness.

Implantable loop recorders (ILR) are currently the option that offers the longest non-interrupted monitoring. Other devices as single-lead surface recorders have also been developed to attain a more extended monitoring than classical 24-48 hour ambulatory Holters. Both types of devices are limited either by signal quality or by computational power, memory and battery. Atrial signals, are more susceptible to noise and they typically require of computationally expensive methods for noise and ventricular activity cancellation. Arrhythmia detection algorithms based on wave morphology are still unrealistic for signals' quality and hardware restrictions of currently available devices. Therefore, they normally rely mainly on cardiac rhythm parameters by R peak detection, more resistant against noise interference [2].

Many algorithms have been proposed for AF detection using only RR interval (RRI) variability; based on statistical dispersion, entropy, symbolic dynamics, time-varying coherence function and Poincaré plot [3]. Many of these studies have proven to be very effective for the detection of AF. However, all of them focused on characterizing and developing a model specific for AF, unable to detect other atrial rhythms [2], [4]–[7]. To the best of our knowledge, there is a lack of methodologies based solely on RRIs capable of identifying tachyarrhythmias other than AF. Nevertheless, also AFL is known to be linked with stroke [8], [9] and AFL, AT and multifocal atrial tachycardia (MAT) with cardiomyopathy caused by rapid atrioventricular conduction. Other atrial electrophysiological disturbances as frequent premature atrial complexes (PAC) previously considered clinically irrelevant, have also been linked to higher stroke incidence, myocardial tissue degradation and AF development [10]–[13]. In addition, maintained atrial bigeminy (AB) has been shown to promote left ventricular remodelling and deterioration [14]. These findings suggest to pay more attention to these conditions whose prevalence should not be ignored. Monitoring exclusively AF may underestimate the influence of other types of tachyarrhythmias and lead to an incomplete evaluation of the cardiac state. Furthermore, frequent PACs and other rhythms that alter the RRI sequence are known to hinder AF detectors as they are confused with AF, increasing false positive rates [15], [3]. Targeting them directly would improve AF detection.

This study poses a new approach towards cardiac tachyarrhythmia classification by transforming RRI into images. Differently than current methodologies, the proposed model can be generalized to different rhythms and, in contrast with AF-focused methods, it does not define rhythm-specific parameters and thresholds. The Poincaré plot is a graphical representation that describes the RRIs non-linear relationships by plotting each RRI against its previous one. Depending on the underlying cardiac rhythm, the plot generated by the RR or dRR intervals follows a diverse pattern that can be visually recognized as described previously in [16], [17]. The proposed methodology is based on the observation that different rhythms

G. García-Isla was with the Department of Electronics, Information and Bioengineering (DEIB), Politecnico di Milano, Milano, MI, 20133 Italy e-mail: guadalupe.garcia@polim.it.

V. Corino and L. Mainardi are with Politecnico di Milano.

Manuscript received April 19, 2005; revised August 26, 2015.

generate different patterns in the plot, and that these can be captured and used to classify other RRIs. Past studies used Poincaré plots for AF detection for defining parameters and thresholds to describe particular patters in the plot [7], [18]–[21]. In this study, we introduce two new versions of the Poincaré plot to which we refer as Poincaré Images and Poincaré Atlases and we explore the possibility of identifying and classifying NSR, AB and AF ECG segments.

Preliminary results considering only a type of Poincaré Image, bin size and time window as well as a simpler classification metric, were presented in [22]. In this work, the concepts of Poincaré Image and Poincaré Atlas are extensively assessed and the parameters influencing their computation are optimized for obtaining better classification results. The improvements introduced in this work with respect to [22] include: the exploration of the bin size influence on Poincaré Images and Altases, the study of different types of Poincaré Images configuration, the optimization of the distance metric between Poincaré Images and Atlases and finally the assessment of the methodology's performance for reduced time windows that range from 120 s to 20 s (in [22] only a time window of 120 s was used). The major contribution of this study is thus, the definition of Poincaré Images and Atlases and the demonstration of their potential to detect and classify different cardiac rhythms with segments as short as 20 s.

II. Materials and methods

The method adopted is based on the analysis of RR intervals and their representation through the Poincaré plots, i.e. the 2-D graph of the current RR versus the previous one. The plot provides a representation of the RR interval dispersion within the RR series and, in a non-linear dynamics view, is the two-dimensional (2-D) reconstructed RR interval phase-space, which is a projection of the reconstructed attractor describing the dynamics of the cardiac system [23], [24]. In this study, the Poincaré plot is treated as an intensity image by introducing the concept of *Poincaré Image* and further computations are performed on it.

A. The Poincaré Image

Let's consider the pairs of two consecutive RR intervals (RR_n, RR_{n+1}), being $n \in \{1, 2, \ldots, N-1\}$ with N the number of samples in the considered epoch. The Poincaré Image, $P[j,k]$ is a pixelated version of the traditional, continuous Poincaré plot and is defined as follows

$$P[j,k] = \sum_{n=1}^{N-1} \mathbf{1}_{[j,\Delta x]}(RR_n) \cdot \mathbf{1}_{[k,\Delta y]}(RR_{n+1}) \quad (1)$$

where $\mathbf{1}_{k,\Delta x}(\cdot)$ is the indicator function

$$\mathbf{1}_{[m,\Delta v]}(x) := \begin{cases} 1 & \text{if } x \in [m\Delta v, (m+1)\Delta v), \\ 0 & \text{if } x \notin [m\Delta v, (m+1)\Delta v). \end{cases} \quad (2)$$

and where k, j are the bin indexes and Δx and Δy are the selected bin size, respectively. Thus, $P[j,k]$ is the counting of the number of times RR_n lays in the interval $[k\Delta x, (k+1)\Delta x)$ and, jointly, RR_{n+1} lays in $[j\Delta y, (j+1)\Delta y)$. The values of $P[j,k]$ are computed in a range of interest and for given values of Δx and Δy. It's worth noting that $P[j,k]$ depends on three parameters: $N, \Delta x, \Delta y$. The Poincaré Image differs from the Poincaré plot because it is discretized in bins and each bin has an associated amplitude. A comparison of the two, for the case of RR segment in NSR, is shown in figure 1.

B. Rhythm classification by Poincaré Image

The basic idea behind the proposed classification strategy is that ECG segments with similar rhythm do share similar Poincaré Images. Mutual Information (MI) metric can be used to measure the similarity between two Poincaré Images: it is a commonly adopted metric to measure similarity between medical images (both 2D and 3D) widely used to evaluate image alignment in image registration problems (Viola et al. [25] and Maes et al. [26]). It measures the amount of information that one variable contains about another one. As a similarity measure it has a number of advantages, as it assumes no prior functional relationship between images. Rather, it assumes a statistical relationship that can be captured by analyzing the images' joint entropy. MI can be expressed through diverse mathematical forms such as Shannon entropy (SE), joint entropy or the Kullball–Leibler distance. Each definition contains the same information and can be rewritten into the others. Based on SE, the MI, $I(A,B)$, between two images A and B, can be expressed as

$$I(A,B) = H(B) - H(B/A) \quad (3)$$

where $H(B)$ corresponds to the SE of image B based on the probability distribution of its pixels' values. $H(B/A)$ instead represents the conditional entropy computed on the conditional probabilities $p(b/a)$ of pixels from image A and B [27]. As there does not exist a defined upper bound for MI, different normalization strategies have been suggested [28], [29]. Normalized MI (NMI) as an analogue to covariance and related with the geometrical mean as in [29] is expressed as

$$NMI(A,B) = \frac{I(A,B)}{\sqrt{H(A)H(B)}} \quad (4)$$

A different approach for measuring dependencies between Poincaré images is the 2D correlation analysis. While MI and NMI evaluate similarities between two images based on their statistical distributions, the 2D correlation coefficient quantifies the energy metric among them. It is computed as

$$Corr(A,B) = \frac{\sum_y \sum_x \left(A_{xy} - \overline{A}\right)\left(B_{xy} - \overline{B}\right)}{\sqrt{\sum_y \sum_x \left(A_{xy} - \overline{A}\right)^2 \sum_y \sum_x \left(B_{xy} - \overline{B}\right)^2}} \quad (5)$$

where x and y are the number of pixels per row and column and $\overline{A}$ and $\overline{B}$ correspond to the mean values of image A and B respectively.

Let's now suppose we know the *characteristic* Poincaré Image for a given cardiac rhythms of interest, i.e. a Poincaré

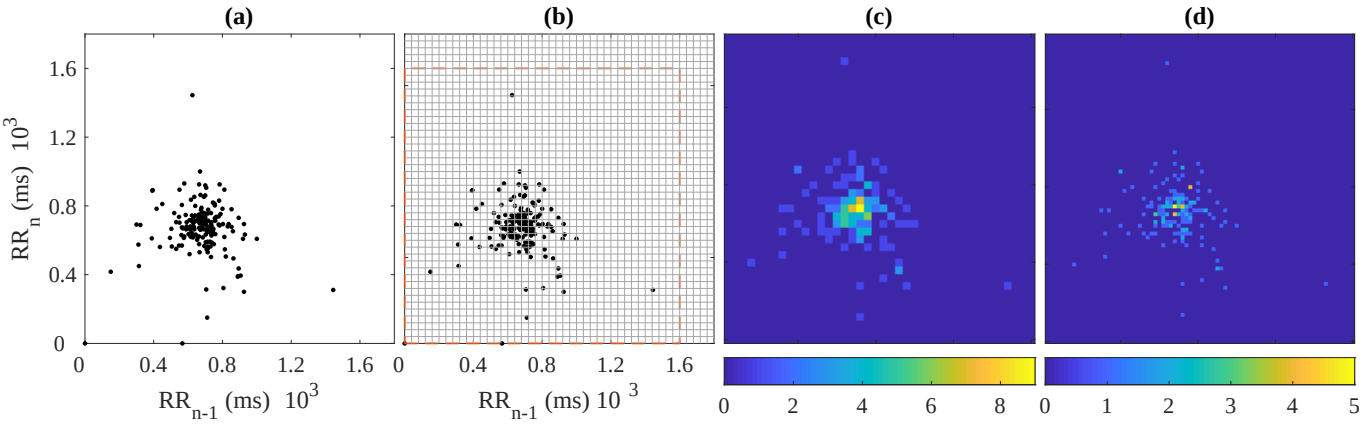

Figure 1. Creation of Poincaré Images from Poincaré Plots.(a) Poincaré Plot obtained from a signal segment of 120 s. (b) Grid indicating the bin discretization of the Poincaré Plot. The discontinuos line accounts for the common limits applied for all Poincaré Images. (c) Poincaré Image created using a bin size of [40x40] ms. (d) Poincaré Image of bin size [20x20].

Image which represents the typical RR pattern for that cardiac rhythm. We will call it *Poincaré Atlas* (the way these Poincaré Atlas are built will be discussed in the next section). Let's A_r be the Poincaré Atlas for rhythms r and let's suppose we are interested in recognizing R different rhythms (let'say, $r = 1$: NSR, $r = 2$: AF, $r = 3$:AT, ... $r = R$: AB). Let's now consider a new RR segment, whose rhythm has to be identified. A strategy could be to compare its Poincaré Image with the all the available Atlases and select the one which maximize the NMI and 2D Correlation coefficient, namely

$$\hat{r}_{NMI} = \underset{0 \leq r \leq R}{\arg\max}\, NMI(A_r, P) \tag{6}$$

$$\hat{r}_{Corr} = \underset{0 \leq r \leq R}{\arg\max}\, Corr(A_r, P) \tag{7}$$

where $\hat{r}$ is now the estimated cardiac rhythm. Note that Equations (6, 7) do not require the setting of any threshold to identify a rhythm. Both parameters could be combined as

$$\hat{r} = \underset{0 \leq r \leq R}{\arg\max} \left(\frac{NMI(A_r, P)}{\hat{r}_{NMI}} \cdot \frac{Corr(A_r, P)}{\hat{r}_{Corr}} \right) \tag{8}$$

The procedure is described in the following figure

In order to apply Equation (8) the set of Atlases had to be computed. Atlases were derived as the average among all the Poincaré Image of the same cardiac rhythm. That is

$$A_r = \frac{1}{M_r} \sum_{m=1}^{M_r} \frac{P_m^{(r)}}{N_m^{(r)}} \tag{9}$$

where $P_m^{(r)}$ is the Poincaré Image of the m^{th} epoch of rhythm r within the available dataset, $N_m^{(r)}$ the total number of RR points in the Poincaré Image and and M_r is the total number of epochs of rhythm r. Prior to the computation of NMI and $Corr$, images were expressed as probability maps as in Equation (9). In addition, in order to discretize values, Poincaré Images and Atlases were scaled to Uint16 before Equation (6).

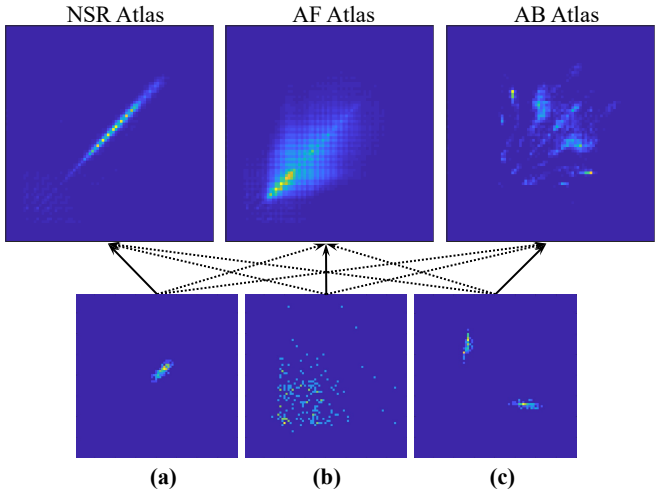

Figure 2. Examples of Poincaré Atlases (first row) and Images (second row) of RR configuration for a time window of 120s and bin size 20ms and rhythms: (a) NSR, (b) AF, (c) AB. Arrows represent the comparison process of NMI and 2D correlation. Solid arrow lines represent the Atlas attaining the maximum value as expressed in 8 for (a),(b) and (c), respectively.

C. Analyzed Datates and Processing

The MIT-BIH arrhythmia database (MITDB), the MIT-BIH atrial fibrillation database (AFDB), and the long term atrial fibrillation database (LTAFDB) were used in this study. The MITDB contains 48 ambulatory half-hour ECG recordings. The AFDB contains 26, 10-hour ambulatory recordings and the LTAFDB 84 recordings of 24–25 hours each [30]. All databases contain beat annotations. From the MITDB and LTAFDB segments labelled as AF, NSR and AB were used. From the AFDB only AF was included. Other rhythms were not considered because either too short episodes or very few episodes were present.

RR sequences were divided into segments of equal length (in s) with 50% overlap. Four window lengths were considered: 120 s, 60 s, 30 s and 20 s. For each segment, three types of Poincaré Images were computed: 1) The RR Poincaré Image, obtained by Equation (1), 2) the dRR Poincaré Image,

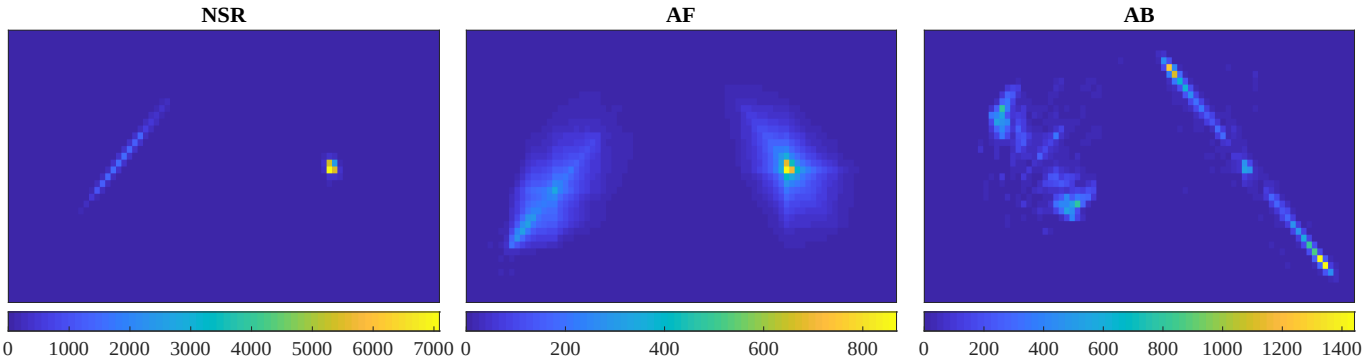

Figure 3. One of the 10 different sets of Poincaré Atlas for $RRdRR$ images computed during the study representing NSR, AF and AB. Values are probability distributions discretized as uint16.

computed by replacing the series of RR intervals in Equation (1) with the series of first difference of the RRs, namely $dRR_n = RR_{n+1} - RR_n$, and, finally 3) the $RRdRR$ Poincaré Images, built by the juxtaposition (side–by–side) of the first two images. All Images were built using the same bin–size on both axes ($\Delta x = \Delta y$). Furthermore, four values of bin–size were tested: 5 ms, 10 ms, 20 ms and 40 ms. In each Image, x– and y-axes ranges were set from 0 ms to 1600 ms for RR Image and from -800 ms to 800 ms for the dRR ones. Images' dimensions (in pixels) varied according to the selected bin–size resulting in a $[320x320]$, $[160x160]$, $[80x80]$ and $[40x40]$ matrix for $\Delta x = 5$ ms, $\Delta x = 10$ ms, $\Delta x = 20$ ms and $\Delta x = 40$ ms, respectively. The combination of the different bin-sizes and window lengths resulted in 16 different configurations that were used to built RR, dRR and $RRdRR$ Images. Each Image was labelled as a determined rhythm (NSR, AF, etc...) according to the dominant cardiac rhythm of the relative RR segment (i.e the dominant rhythm was the rhythm that covered more than the 50% of the signal segment used to build the Poincaré Image). From all the images generated, only those labelled as NSR, AF or AB were considered.

D. Performance evaluation

The available Poincaré Image dataset was divided in two subsets by patient–wise division, i.e. each subset contained images of different patients: the training–set (containing 80% of the available patients) and the independent test–set (containing the remaining 20% ones). The training–set Images were used to generate the Atlases for each rhythm by averaging (Equation (9)) all the available images belonging to the same cardiac rhythm. Then, for each image of the test–set, the NMI and 2D Correlation coefficient between the image and the Atlases were computed and the rhythm identified according to Equation (8). A ten fold cross–validation was performed to avoid bias related to a single split of the dataset. Given the low and unequal distribution of AB images, AB patients were divided as homogeneously as possible in the ten—fold cross–validation sets. At each K–fold, 8 subsets were used for train and 2 for test. Results are expressed as weighted mean and standard deviation with respect to the number of classified segments at each iteration.

III. Results

The total amount of images generated for the three rhythms is displayed in Table I. The last column of the table indicates the total number of different patients from which the images of each rhythm came from.

Table I
TOTAL NUMBER OF IMAGES AND PATIENTS PER RHYTHM.

Rhythm	Time Window (s)				Patients
	120	60	30	20	
NSR	52,000	103,800	207,100	309,800	113
AF	41,670	83490	167,100	250,800	114
AB	211	530	1303	2,251	30

A. Image choice

To choose the best image type (RR, dRR and $RRdRR$) accuracy, sensitivity and specificity classification values were compared for different window lengths and bin–sizes. As an example the performance for AF classification is shown in Table II. For AF classification, the usage of RR images led to higher specificity but poorer sensitivity values than the usage of dRR images. The combination of both in $RRdRR$ led to a more balanced relationship between sensitivity and specificity maintaining similar accuracy values than dRR. Therefore, the following results are shown for $RRdRR$ only.

B. Distance metric for Poincaré Image classification

Accuracy, sensitivity and specificity values of the $RRdRR$ images classification after the 10 fold cross-validation are gathered in Figures 4, 5 and 6. In each figure, each row of three graphs represents a rhythm's classification results using different time windows and bin–sizes. Each line in a graph represents the results obtained using the same time window with varying bin–sizes along the x-axis.

Figures 4, 5 and 6 gather the classification results obtained using NMI, 2D correlation and the combination of both, respectively, distance metrics between Poincaré Images and the rhythm–specific Atlases. The combination of NMI and 2D correlation as represented in Figure 6 led to a better performance than both measures independently. Therefore,

Table II
RESULTS FOR THE ALL TYPES OF AF IMAGES, TIME WINDOWS AND BIN SIZE 40 ms.

	TW (s)	RR	dRR	RRdRR
Accuracy (%)	120	82.32±5.27	89.26±3.83	89.96±3.52
	60	83.15±4.79	89.09±3.23	89.78±3.24
	30	82.39±4.20	88.18±2.79	89.12±3.19
	20	82.52±3.21	87.18±3.24	88.60±3.05
Sensitivity (%)	120	82.75±8.98	95.61±4.35	94.87±3.71
	60	83.52±9.40	95.15±3.84	94.35±3.68
	30	81.77±6.35	94.43±1.91	93.40±2.95
	20	80.70±6.29	92.20±1.93	91.76±3.03
Specificity (%)	120	81.93±4.29	83.39±4.50	85.43±4.06
	60	82.78±7.89	83.45±7.65	85.52±7.46
	30	82.96±7.71	82.36±6.25	85.13±7.46
	20	84.20±6.98	82.49±7.14	85.63±6.83

Values are presented as weighted mean ± standard deviation.

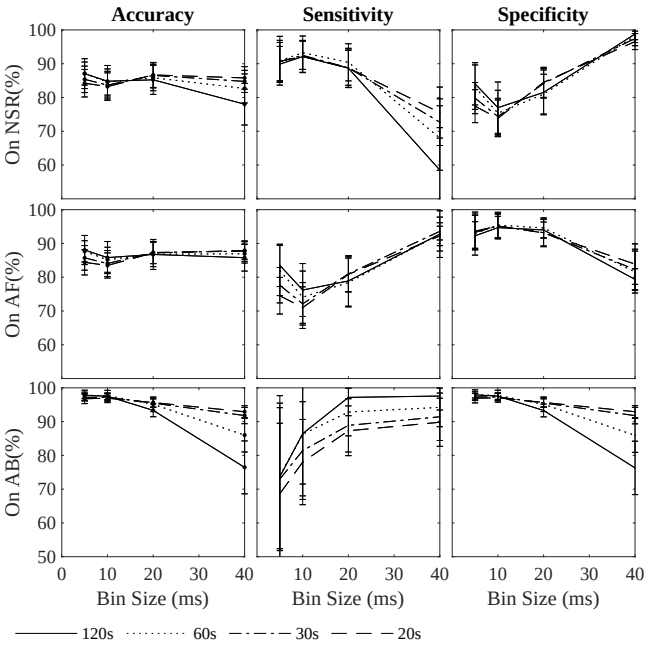

Figure 4. Results for NMI as distance metric. Accuracy, sensitivity and specificity values for the classification of NSR, AF and AB as a function of time windows and bin sizes. NSR, AF and AB are shown from the top to the bottom.

further results are presented and discussed just using this combined metric as described in Equation 8.

C. Image parameter optimization

Independently of the bin size, the larger the time window, the better the classification performance of AF and NSR. As the time window was reduced, so was the standard deviation for all rhythms.

The underrepresentation of AB, led to very high accuracy values and higher standard deviation with respect to AF and NSR. Sensitivity values for a time window of 120 s showed a poorer performance in comparison to the other time windows used due to the lower amount of AB images. Bin size did not influence substantially results in term of accuracy values

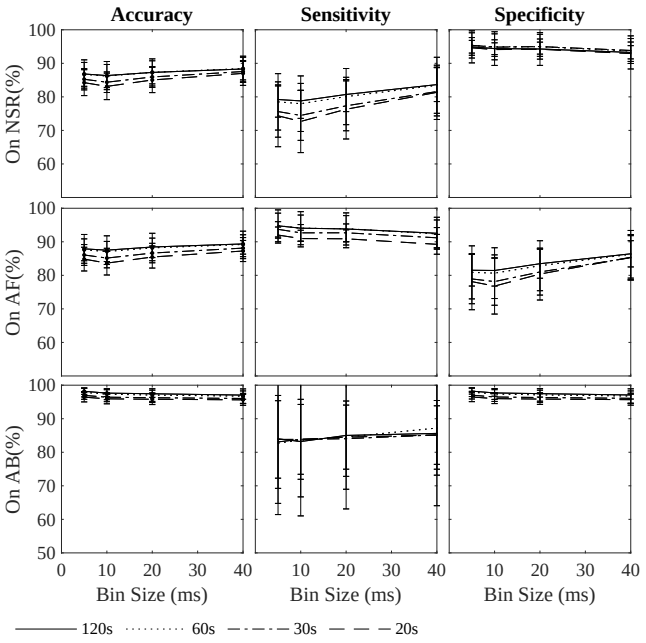

Figure 5. Results for 2D correlation as distance metric. Accuracy, sensitivity and specificity values for the classification of NSR, AF and AB as a function of time windows and bin sizes. NSR, AF and AB are shown from the top to the bottom.

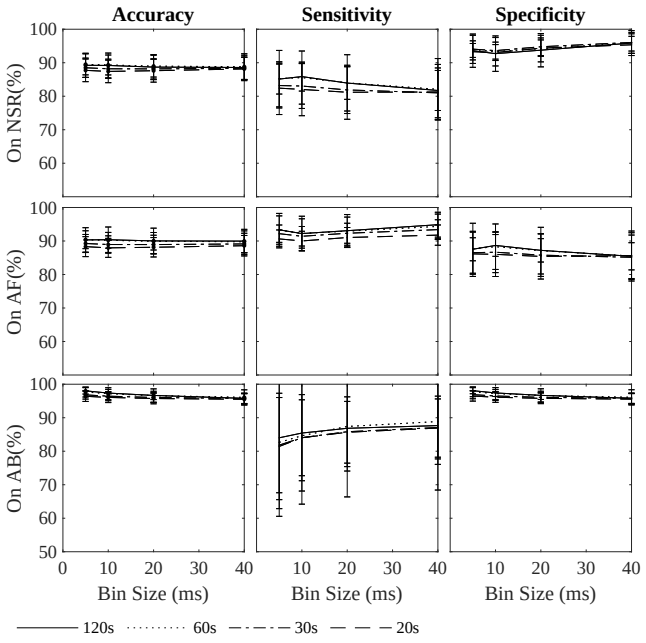

Figure 6. Results for NMI and 2D correlation as distance metric. Accuracy, sensitivity and specificity values for the classification of NSR, AF and AB as a function of time windows and bin sizes. NSR, AF and AB are shown from the top to the bottom.

for AF and NSR. However, it did affect the balance between sensitivity and specificity values of AF and NSR.

D. Statistical analysis

A two-way ANOVA test was performed to study time window and bin size influence in the classification of NSR, AF and AB. Time window was significant for AF and AB

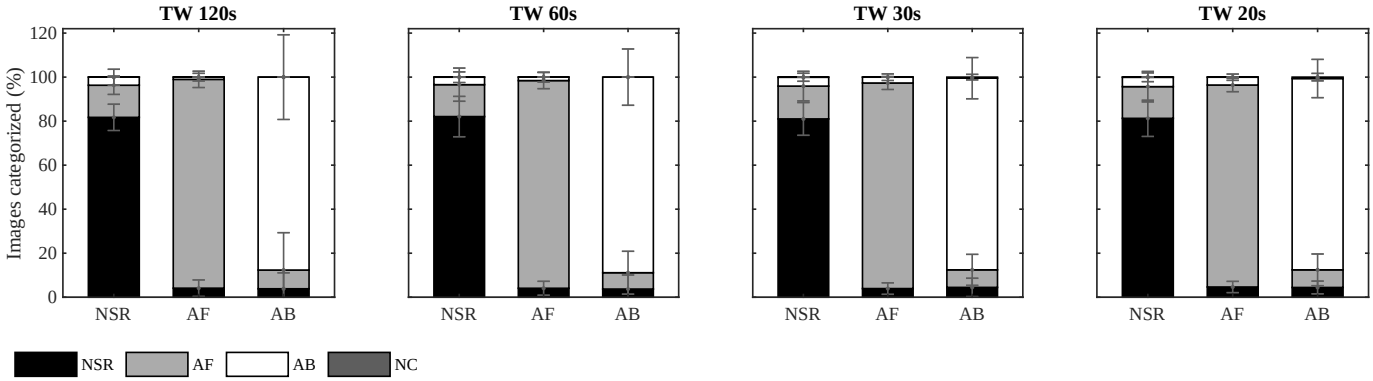

Figure 7. Classification results after ten fold cross validation of the three time windows and bin–size [40x40] ms. Each bar represents in percentage, the distribution of the classification of all images with a determined rhythm; NSR, AF or AB, into one of the three rhythms or non classified (NC).

sensitivity and specificity values respectively ($p < 0.05$), 120 s and 60 s the best options for both cases. Bin size was only significant for NSR specificity, being 40 ms the best choice. Based in this analysis, the best combination of parameters would be a 120 or 60 s time window with 40 ms bin size. Results for this combination are gathered in Table III.

Table III
CLASSIFICATION RESULTS WITH TIME WINDOW 60 S AND BIN SIZE 40 MS.

Rhythm	Accuracy (%)	Sensitivity (%)	Specificity (%)
NSR	88.81±3.87	82.07±9.18	95.91±3.14
AF	89.78±3.24	94.35±3.68	85.51±7.46
AB	96.08±2.25	88.86±12.78	96.10±2.25

Values are presented as weighted mean ± standard deviation.

E. Optimized ECG classification

In Figure 7 the classification distribution of the Poincaré Images for the four different time windows and optimal bin–size is shown. Images were labelled as "not classified" when the score resulting from the computation of NMI and 2D correlation was the same for more than one Poincaré Atlas. Each bar of the graphs represents the 100% of images of a determined rhythm and the percentage that has been classified into each of the four different categories; NSR, AF, AB or not classified (NC). Regardless of the time window and bin–size used, the classification distribution of each different set of images belonging to the same rhythm followed similar patterns. The misclassified NSR images were always categorized as false AF episodes in a higher percentage than AB episodes. AF false negatives were although classified more often as NSR than as AB. AB classification after ten fold cross-validation attained higher standard deviation values with respect to the other rhythms of study. However, as the time window was shortened and the amount of AB images increased, the standard deviation was reduced.

IV. DISCUSSION

Poincaré plots have been used as inspiration for the generation of parameters to describe non–linear RRI patterns, typically focusing on the detection of AF [2], [5], [7], [21]. However, to the best of our knowledge, this is the first study that considered the design represented in the plot as a whole. The creation of a reference image specific for each rhythm aimed to capture the general design created by that rhythm as described by [16] even influenced by different noise levels presence, ectopic beats, heart rate or inter–patient variability.

AF, NSR and AB rhythms were used to test the presented methodology. As AB episodes are shorter and more infrequent in the databases than AF and NSR, the number of images and patients was inferior to those of the other two rhythms of study. Different databases were used to maximize variability between the signals employed. Noisy signal segments were not excluded from this study. From the three types of Poincaré Images studied, the combination of RR and dRR in $RRdRR$ led to a balanced relationship between AF sensitivity and specificity. Even though both RR and dRR have been used in several past studies [7], [18], [21], $RRdRR$ has never been reported before. Time windows of 120 s and 60 s were the best options according to the statistical analysis. This is compliant with the European Society of Cardiology (ESC) AF guidelines which set 30 s as the minimum length for an AF episode to be considered clinically relevant [31]. In the presented methodology, a time window of 60 s would detect $>$30 s episodes, as only the 50% of arrhythmia prevalence on the time window's samples is needed for its detection.

The condition of $>$30 s AF episodes is based on an agreed convenience due to the limitations of current monitoring techniques rather than on an electrophysiological basis. The significance of shorter episodes still remains unclear. Hence, their monitoring could be of clinical interest. Results obtained for 30 s and 20 s did not differ more than 3 percentage points from those of wider time windows as presented in Table II and Figure 6. Even if better performance was achieved for larger time windows, shorter ones as 20 s and 30 s could be of greater interest from a clinical perspective. The aim of presenting different time windows was not only to optimize this parameter, but also to study how the methodology behaves as it is shortened.

AF and NSR results suggest Poincaré Atlases and Images manage to represent the complex RRI dynamics characteristic

of a certain rhythm. Standard deviation values instead, show the dependency of the methodology on the patients used both for classification and for computation of the Atlases. This may indicate than either more than one Atlas may be needed to successfully capture all the different types of behaviour of AF and NRS or than more patients are required to fully represent the heterogeneity of the RR patterns characteristic of a certain rhythm. AF for instance, is known to present different degrees of organization [32] that may lead to different RRI behaviour. Furthermore, the high standard deviation obtained for AB classification clearly shows that the AB inter–patient variability was not enough to provide a complete representation of AB pattern for all cases. Lower sensitivity values obtained in some K–fold iterations as 56.8%, 65.4% and 70.0% with corresponding specificity 98.3%, 99.4% and 99.0% suggest that the atlases created did not succeed in representing the AB pattern of the test set population. However, high sensitivity values as 97.7%, 96.7% or 94.6% with specificity 98.7%, 96.1% and 96.7% demonstrate that the Poincaré Atlas approach may successfully discriminate among AF, NSR and AB. These results point out also at the necessity of the proposed methodology of a higher number of patients and episodes to build a rhythm–specific Atlas.

Nevertheless, with the enough amount of patients and episodes RRI analysis using Poincaré Images would permit the generalization of the method to different cardiac rhythms, in contrast with current algorithms that are rhythm–specific designed.

A. Related work

Other studies aiming to classify cardiac tachyarrhythmia only through RRI analysis attempted to characterize a particular rhythm behaviour with one or more parameters and set a threshold indicating the presence of such rhythm [2], [4], [5], [7], [15], [18], [21], [33]–[35]. Those studies targeted a single tachyarrhythmia and proved to be very effective at detecting AF. However, they reported poor results when trying to detect other rhythms as [2], [7].

A comparison of the former approach with the published algorithms is rather challenging as current algorithms have been optimized for the detection of AF while the one presented in this work aims to target other rhythms simultaneously. Contrast among them has been typically done by studying AF detection on the AFDB. However, the AFDB does not contain annotations for rhythms other than AF, AV junctional rhythm and AFL, being these last two in a very low proportion. Therefore, it is difficult to evaluate how other detector's performance is influenced by the presence of other rhythms and how our results could improve by targeting them.

Lee et al. [34] published a methodology for AF detection based on time varying coherence functions (TVCF) and sensitivity They reported a sensitivity and specificity of 98.2% and 97.7% respectively on the AFDB. However, when their method was tested on the MIT-BIH arrhythmia database, that contains other arrhythmia, specificity lowered from 97.7% to 81.2%. The thresholds computed for the detection of AF were calculated using the same AFDB database, so performance results using this database could be biased. Zhoe et al [5] used symbolic dynamics and SE for AF detection, obtaining a sensitivity and specificity of 97.4% and 98.4% on the AFDB. Similarly to [34], their specificity dropped from 98.28% in the AFDB to 87.41% in the MIT-BIH arrhythmia database. Petrenas et al. [33] AF detector for an 8-beat window achieved a sensitivity and specificity of 97.1% and 98.3% respectively on the AFDB. One of the key points for the achievement of such performance was the implementation of a bigeminy and ectopic beat suppression algorithm. They also reported a decrease in specificity when applied to the MIT-BIH database from 98.3% to 86.4%.

These differences in performance show how explicitly tackling other rhythms could improve AF monitoring. In addition, they demonstrate that the high specificity rates reported on AFDB might not be representative of AF detection in presence of other arrhythmia. The former study does not intent to present an specific classifier for AF and AB, but to introduce a new type of approach towards the detection of atrial tachyarrhythmia. It aims to put forward a method that could be extended to different types of RRI patterns rather than a model specifically designed to detect a single arrhythmia.

B. Limitations and future work

The major limitation of this study is the need of a considerable amount of tachyarrhythmia episodes and patients to create the Poincaré Atlases. Some data augmentation techniques could help overcome this issue. However, the resultant images should still be physiologically feasible as otherwise the effect could be counterproductive. Geometrical modification techniques implying image transformations as rotation and flipping would not fulfil this condition unless values representing RR intervals are kept withing the physiological range. Although we theorise that the proposed model could be applied to describe other rhythms, the available data limited the study to AF, NSR and AB. Furthermore, the amount of AB data was very low in comparison with AF and NSR, which led to a very high standard deviation values. Ideally, a set of Poincaré Atlases should be built representing all different tachyarrhythmia and made open-source for being used in other studies.

V. Conclusion

This paper presents a new approach for cardiac tachyarrhythmia classification introducing the concepts of Poincaré Images and Atlases for the creation of different rhythm reference models. In addition, a combined display of the RR and dRR Poincaré Plot, $RRdRR$, has been introduced for the joint description of the two-beat and three-beat variability. The proposed method has been evaluated for the detection of AF, AB and NSR segments with promising results, proving the capacity of extending it to different rhythms.

Acknowledgment

This project is framed inside MY-ATRIA consortium. MY-ATRIA project has received funding from the European Union's Horizon 2020 research and innovation programme under the Marie Skłodowska-Curie grant agreement No.766082

REFERENCES

[1] T. V. Glotzer, E. G. Daoud, D. G. Wyse, D. E. Singer, M. D. Ezekowitz, C. Hilker, C. Miller, D. Qi, and P. D. Ziegler, "The Relationship between daily atrial tachyarrhythmia burden from implantable device diagnostics and stroke risk the trends study," *Circulation: Arrhythmia and Electrophysiology*, vol. 2, no. 5, pp. 474–480, 2009.

[2] D. E. Lake and J. R. Moorman, "Accurate estimation of entropy in very short physiological time series: the problem of atrial fibrillation detection in implanted ventricular devices," *AJP: Heart and Circulatory Physiology*, vol. 300, no. 1, pp. H319–H325, 2011.

[3] L. Sörnmo, A. Petr, V. Marozas, and P. E. C. G. Databases, "Atrial Fibrillation from an Engineering Perspective," pp. 49–71, 2018. [Online]. Available: http://link.springer.com/10.1007/978-3-319-68515-1

[4] J. Lee, B. A. Reyes, D. D. McManus, O. Mathias, and K. H. Chon, "Atrial fibrillation detection using an iphone 4S," *IEEE Transactions on Biomedical Engineering*, vol. 60, no. 1, pp. 203–206, 2013.

[5] X. Zhou, H. Ding, W. Wu, and Y. Zhang, "A real-time Atrial fibrillation detection algorithm based on the instantaneous state of heart rate," *PLoS ONE*, vol. 10, no. 9, 2015.

[6] A. Petrėnas, L. Sörnmo, A. Lukoševičius, and V. Marozas, "Detection of occult paroxysmal atrial fibrillation," pp. 287–297, 2015.

[7] S. Sarkar, D. Ritscher, and R. Mehra, "A detector for a chronic implantable atrial tachyarrhythmia monitor," *IEEE Transactions on Biomedical Engineering*, vol. 55, no. 3, pp. 1219–1224, 2008.

[8] J. A. Cairns, S. Connolly, S. McMurtry, M. Stephenson, and M. Talajic, "Canadian Cardiovascular Society atrial fibrillation guidelines 2010: Prevention of stroke and systemic thromboembolism in atrial fibrillation and flutter," *Canadian Journal of Cardiology*, vol. 27, no. 1, pp. 74–90, 2011.

[9] N. S. Sawhney and G. K. Feld, "Diagnosis and Management of Typical Atrial Flutter," *Medical Clinics of North America*, vol. 92, no. 1, pp. 65–85, 2008.

[10] B. T. Huang, F. Y. Huang, Y. Peng, Y. B. Liao, F. Chen, T. L. Xia, X. B. Pu, and M. Chen, "Relation of premature atrial complexes with stroke and death: Systematic review and meta-analysis," *Clinical Cardiology*, vol. 40, no. 11, pp. 962–969, 2017.

[11] B.-h. Chong, V. Pong, K.-f. Lam, S. Liu, M.-l. Zuo, Y.-f. Lau, C.-p. Lau, H.-f. Tse, and C.-w. Siu, "Frequent premature atrial complexes predict new occurence of atrial fibrillation and adverse cardiovascular events," *Europace*, vol. 14, pp. 942–947, 2011.

[12] Z. Binici, T. Intzilakis, O. W. Nielsen, L. Køber, and A. Sajadieh, "Excessive supraventricular ectopic activity and increased risk of atrial fibrillation and stroke," *Circulation*, vol. 121, no. 17, pp. 1904–1911, 2010.

[13] B. S. Larsen, P. Kumarathurai, J. Falkenberg, O. W. Nielsen, and A. Sajadieh, "Excessive Atrial Ectopy and Short Atrial Runs Increase the Risk of Stroke beyond Incident Atrial Fibrillation," *Journal of the American College of Cardiology*, vol. 66, no. 3, pp. 232–241, 2015.

[14] C. F. Pacchia, N. W. Akoum, S. Wasmund, and M. H. Hamdan, "Atrial bigeminy results in decreased left ventricular function: An insight into the mechanism of PVC-induced cardiomyopathy," *PACE - Pacing and Clinical Electrophysiology*, vol. 35, no. 10, pp. 1232–1235, 2012.

[15] P. Langley, M. Dewhurst, L. Y. Di Marco, P. Adams, F. Dewhurst, J. C. Mwita, R. Walker, and A. Murray, "Accuracy of algorithms for detection of atrial fibrillation from short duration beat interval recordings," *Medical Engineering and Physics*, vol. 34, no. 10, pp. 1441–1447, 2012. [Online]. Available: http://dx.doi.org/10.1016/j.medengphy.2012.02.002

[16] H. D. Esperer, C. Esperer, and R. J. Cohen, "Cardiac arrhythmias imprint specific signatures on Lorenz plots," *Annals of Noninvasive Electrocardiology*, vol. 13, no. 1, pp. 44–60, 2008.

[17] T. Anan, K. Sunagawa, H. Araki, and M. Nakamura, "Arrhythmia analysis by successive RR plotting," *Journal of Electrocardiology*, vol. 23, no. 3, pp. 243–248, 1990.

[18] J. Park, S. Lee, and M. Jeon, "Atrial fibrillation detection by heart rate variability in Poincare plot," *BioMedical Engineering Online*, vol. 8, pp. 1–12, 2009.

[19] C. K. Karmakar, A. H. Khandoker, J. Gubbi, and M. Palaniswami, "Complex correlation measure: a novel descriptor for Poincaré plot." *Biomedical engineering online*, vol. 8, p. 17, 2009.

[20] L. Zhang, T. Guo, B. Xi, Y. Fan, K. Wang, J. Bi, and Y. Wang, "Automatic recognition of cardiac arrhythmias based on the geometric patterns of poincaré plots," *Physiological Measurement*, vol. 36, no. 2, pp. 283–301, 2015.

[21] J. Lian, L. Wang, and D. Muessig, "A simple method to detect atrial fibrillation using RR intervals," *American Journal of Cardiology*, vol. 107, no. 10, pp. 1494–1497, 2011.

[22] G. García-Isla, V. D. Corino, and L. T. Mainardi, "Cardiac Tachyarrhythmia Detection by Poincaré Plot-Based Image Analysis," in *Computing in Cardiology*, Singapore, 2019.

[23] M. Brennan, M. Palaniswami, and P. Kamen, "Distortion properties of the interval spectrum of IPFM generated heartbeats for heart rate variability analysis," *IEEE Transactions on Biomedical Engineering*, vol. 48, no. 11, pp. 1251–1264, 2001.

[24] ——, "Poincaré plot interpretation using a physiological model of HRV based on a network of oscillators," *American Journal of Physiology - Heart and Circulatory Physiology*, vol. 283, no. 5, pp. H1873–H1886, 2002. [Online]. Available: http://ajpheart.physiology.org/lookup/doi/10.1152/ajpheart.00405.2000

[25] P. Viola and W. I. William M., "Alignment by Maximization of Mutual Information," *International Journal of Computer Vision*, vol. 24, no. 2, pp. 137–154, 1997.

[26] F. Maes, A. Collignon, D. Vandermeulen, G. Marchal, and P. Suetens, "Multi-modality image registration by maximization of mutual information," *Proceedings of the Workship on Mathematical Methods in Biomedical Image Analysis*, vol. 16, no. 2, pp. 14–22, 1996.

[27] J. Pluim, "Mutual information based registration of medical images," *Ponsen & Looijen*, vol. XX, pp. 1–21, 2000.

[28] C. Studholme, D. L. Hill, and D. J. Hawkes, "An overlap invariant entropy measure of 3D medical image alignment," *Pattern Recognition*, vol. 32, no. 1, pp. 71–86, 1999.

[29] A. Strehl and J. Ghosh, "Cluster ensembles - A knowledge reuse framework for combining multiple partitions," *Journal of Machine Learning Research*, vol. 3, no. 3, pp. 583–617, 2003.

[30] A. L. Goldberger and L. A. N. Amaral, "PhysioBank, PhysioToolkit, and PhysioNet," *Circulation*, vol. 101, no. 23, pp. 215–220, 2012.

[31] P. Kirchhof et al., "2016 ESC Guidelines for the management of atrial fibrillation developed in collaboration with EACTS," *European Heart Journal*, vol. 37, no. 38, 2016.

[32] G. W. Botteron and J. M. Smith, "Quantitative assessment of the spatial organization of atrial fibrillation in the intact human heart," *Circulation*, vol. 93, no. 3, pp. 513–518, 1996.

[33] A. Petrenas, V. Marozas, and L. Sörnmo, "Low-complexity detection of atrial fibrillation in continuous long-term monitoring," *Computers in Biology and Medicine*, vol. 65, pp. 184–191, 2015.

[34] J. Lee, Y. Nam, D. D. McManus, and K. H. Chon, "Time-varying coherence function for atrial fibrillation detection," *IEEE Transactions on Biomedical Engineering*, vol. 60, no. 10, pp. 2783–2793, 2013.

[35] S. Dash, K. H. Chon, S. Lu, and E. A. Raeder, "Automatic real time detection of atrial fibrillation," *Annals of Biomedical Engineering*, vol. 37, no. 9, pp. 1701–1709, 2009.